Journal of

Applied and Computational Mechanics

Shahid Chamran
University of Ahvaz

Research Paper

Impact of Geometrical Parameters on Indoor Environments with Single-Sided Ventilation: Experimental and Numerical Study

Hasna Abid[1,2] , Ridha Djebali[3] , Hamza Faraji[4] , Mariem Lajnef[1] , Zied Driss[1] , Jamel Bessrour[2]

[1] University of Sfax, Laboratory of Electro-Mechanic Systems (LASEM), National School of Engineers of Sfax (ENIS), B.P. 1173, km 3.5 Road Soukra, 3038 Sfax, Tunisia

[2] University of Tunis Manar, National School of Engineers of Tunis (ENIT), BP 37, le Belvedere, 1002 Tunis, Tunisia

[3] UR: Modeling, Optimization and Augmented Engineering, ISLAI Béja, University of Jendouba, Béja 9000, Tunisia

[4] National School of Applied Sciences, Cadi Ayyad University, Marrakech, Morocco

Abstract. This paper presents a comprehensive investigation into the impact of geometrical parameters on indoor environments. The study utilizes an experimental setup and a developed numerical model, with validation achieved through comparison with test data from a cabin prototype, focusing on air velocity and temperature profiles. The numerical model undergoes optimization, including turbulence and grid independence analyses, to ensure accurate simulations. Additionally, the study explores the heat source effect on indoor thermal comfort through a series of numerical simulations. Based on the combined numerical and experimental findings, the study establishes robust correlations to explain the variations resulting from these factors. It highlights the crucial roles of roof height and room length in determining aerodynamic characteristics within the room. The study's comparative analysis shows that the Predicted Mean Vote (PMV) remains below 0.45 for a heat flux of 150 W.m^{-2}, indicating a neutral thermal sensation. In contrast, it rises to 2.55 for a heat flux of 800 W.m^{-2}, indicating a warm thermal sensation. Overall, this research provides valuable insights into the complex dynamics of airflow within indoor environments.

Keywords: Geometrical parameters, Indoor environments, Experimental setup, Numerical model, Thermal comfort.

1. Introduction

In today's context, ensuring thermal comfort has emerged as the foremost priority for occupants within indoor environments [1]. The maintenance of superior air quality and the provision of optimal thermal conditions in indoor spaces are indispensable for both occupant well-being and productivity in work settings [2]. Consequently, HVAC (Heating, Ventilation, and Air Conditioning) systems are essential in meeting the thermal requirements of indoor spaces [3]. In pursuit of this goal, numerous investigations have been carried out to identify the factors that influence interior environments and, by extension, indoor thermal satisfaction. A significant quantity of research has been dedicated to examining the impact of opening positions and quantities. Notably, Li et al. [4] as well as Shetabivash [5] have delved into the repercussions of openings. Their findings underscore that the shape and placement of openings significantly influence the airflow patterns within indoor environments. Moreover, extensive literature reviews have been undertaken to evaluate the impact of building geometry on thermal satisfaction. Consequently, indoor distributions have been scrutinized in diverse building-scale designs. For instance, Farouk [6] conducted a numerical assessment of thermal comfort in high-rise buildings, achieving commendable concurrence between the results of the numerical model and those obtained by others. Similarly, Montazeri, Blocken, Derome, Carmeliet, and Hensen [7] carried out a numerical investigation, exploring the effects of building size and geometry. This investigation encompassed three distinct scenarios: buildings with identical height (H) and width (W), buildings with (H) > (W), and buildings with (H) = (W). Additionally, the inclination of the roof constitutes another crucial parameter that exerts a notable effect on the distribution of interior air. Driss et al. [8] employed the s k-ε turbulence model to investigate the height impact of an inclined roof obstacle, revealing that roof height directly influences local characteristics. In a similar vein, Peren et al. [9] conducted a numerical investigation involving five distinct roof inclination angles, noting that the greatest inclination angle resulted in the maximum air velocity. In the context of the parameters, it is imperative to consider the assessment of thermal comfort. The predicted mean vote (PMV) and the predicted percentage of dissatisfied (PPD) are thermal satisfaction indicators introduced by Fanger and Toftum [10] and standardized by ISO 7730 [11] play a pivotal role. Ahmed et al. [12] utilized the PPD and PMV satisfaction indices to assess the influence of the placement of exhaust diffusers on thermal well-being within an office room. Their findings indicated that thermal comfort was enhanced when room heat sources, such as ceiling lamps, were combined with exhaust

outlets. Furthermore, Abid et al. [13] explored the effect of the incoming velocity on thermal satisfaction using the PMV and PPD indicators, observing that increased incoming velocity could induce a cool sensation. In a different context, Chen et al. [14] employed a CFD simulation to investigate thermal satisfaction in a kitchen environment, affirming that PMV values were contingent on the exhaust volume of the range hood. Meanwhile, Chaiyapinunt and Khamporn [15] studied the influence of solar radiation on overall thermal satisfaction and localized thermal satisfaction conditions within a building situated in a tropical climate. Their findings suggested that moving away from the glass window improved the thermal well-being of individuals seated in the space. The existing literature has notably lacked correlation equations that establish a connection between geometrical parameters, such as cabin length and cabin roof height, and various indoor airflow characteristics. The primary goal of this paper is to bridge this knowledge gap by providing correlation equations that elucidate the relationship between these geometrical parameters and key airflow characteristics. These equations have been derived through a fitting method based on the results obtained from our simulations. Consequently, this work confirms the direct impact of geometrical parameters on the Predicted Mean Vote (PMV), thereby offering valuable insights into airflow behavior within indoor environments. To achieve this objective, CFD simulations have been conducted through the ANSYS Fluent 17.0 commercial Computational Fluid Dynamics (CFD) software. This paper is structured into seven sections: First section provides a thorough analysis of the literature of various parameters affecting interior environments and thermal satisfaction. Second section introduces the cabin and outlines the approach employed in the experimental configuration. Third section presents a detailed information on the box prototype's geometric configuration and the selection of numerical parameters. Fourth section highlights the CFD results pertaining to velocity fields, temperature distributions, total pressure, and turbulent kinetic energy inside the box prototype, thereby investigating the impact of geometrical parameters. Fifth section explores the impact of geometrical parameters on interior thermal satisfaction, shedding light on their significance in this context. Sixth section contrasts the numerical outcomes with the experimental findings to assess the reliability of the CFD simulations. Seventh section serves as the work's conclusion by summarizing the main results and contributions of this research endeavor. In essence, this paper seeks to fill a critical void in the existing knowledge by establishing correlations between geometrical parameters and indoor airflow characteristics, with a particular focus on their impact on thermal comfort.

2. Experimental Procedure

Figure 1 illustrates the cabin prototype under consideration, featuring measurement of 1.88 m x 1 m x 1.45 m (length x width x height). This study shares similarities with the work of Karava et al. [16], who investigated wind-induced cross ventilation in a generic isolated building model featuring asymmetric opening positions. The building model in their study had dimensions of 0.1 m x 0.1 m x 0.08 m (W x D x H, 1:200 scale), corresponding to full-scale dimensions of 20 m x 20 m x 16 m.

This cabin incorporates two apertures with a uniform diameter equal to 0.1 m, strategically positioned at the plane identified by $y = 0.5$ m, as depicted in Fig. 1(a). In this study, we deliberately selected a single-sided ventilation configuration due to its numerous advantages, as detailed by Zhong et al. [17]. This configuration offers efficient airflow control, particularly in managing indoor air quality and temperature. Additionally, it simplifies the design and operation of ventilation systems, making it a practical choice for various building types and climates. Furthermore, single-sided ventilation is known to enhance energy efficiency by minimizing heat loss or gain, thereby contributing to sustainable building practices. The walls of the cabin exhibit a thermal conductivity equal to 0.061 $W.m^{-1}.K^{-1}$. Throughout this study, all measurements were conducted under steady-state conditions, ensuring that a sufficient duration had elapsed for stable conditions to prevail. The primary objectives of these measurements were to ascertain the boundary conditions required for CFD simulations and to collect data at various designated points (as illustrated in Fig. 1(a)). To facilitate these measurements, we created distinct openings with a diameter of 16 mm on the lateral surface of the cabin. These openings served as access points for inserting hot-wire anemometer sensors of the AM 4204 type, enabling us to determine the associated velocity values. In fact, this device can measure low air velocities ranging from 0.2 to 20 $m.s^{-1}$ with a resolution of 0.1 $m. s^{-1}$.

3. Numerical Model

The process for numerical modeling and validating cabin simulations with ANSYS 17.0 consists of three main stages: pre-processing, solving, and post-processing. In the pre-processing stage, the cabin geometry is developed using ANSYS Design Modeler, followed by meshing the geometry using the ANSYS Meshing Application. The solving stage entails assigning materials to the cabin and setting boundary conditions based on the experimental setup. The Reynolds-Averaged Navier-Stokes (RANS) equations are then solved. Finally, in the post-processing stage, numerical results are presented within ANSYS FLUENT and CFD-Post. The results are analyzed and presented graphically to aid interpretation once the simulation is complete.
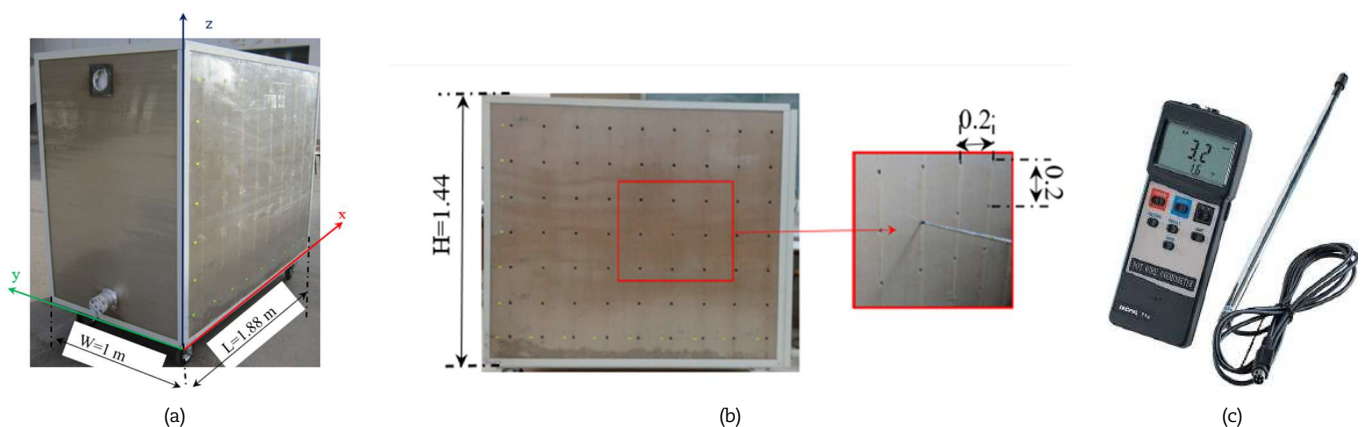

(a)   (b)   (c)

Fig. 1. Experimental procedure, (a) presentation of the cabin prototype, (b) presentation of the measurement points, (c) an anemometer of the Hot-wire type.

3.1. Governing equations

The focus of this section is on the governing equations utilized in this study to model turbulent incompressible flow, which include the steady-state Reynolds-averaged Navier-Stokes (RANS) equations for the conservation of mass and momentum [18-20].

The continuity equation is written as follows:

$$\frac{\partial}{\partial x_i}(\rho u_i) = 0 \tag{1}$$

The momentum equations are written as follows:

$$\frac{\partial}{\partial x_j}(\rho u_i u_j) = -\frac{\partial p}{\partial x_i} + \frac{\partial}{\partial x_j}\left[\mu\left(\frac{\partial u_i}{\partial x_j} + \frac{\partial u_j}{\partial x_i}\right)\right] + \frac{\partial}{\partial x_j}(-\rho \overline{u_i' u_j'}) \tag{2}$$

where ρ represents the density (kg.m^{-3}), p denotes the pressure (Pa), μ presents the dynamic molecular viscosity (kg.m^{-1}.s^{-1}), x_i presents the cartesian coordinate (m) for $i = 1,2,3$, u_i presents the velocity component in the x_i direction (m.s^{-1}), δ_{ij} presents the Kronecker delta and $\rho \overline{u_i' u_j'}$ presents the Reynolds stresses.

The approach adopted follows the Boussinesq hypothesis connecting the Reynolds stresses with mean velocity gradients:

$$-\rho \overline{u_i' u_j'} = \mu_t\left(\frac{\partial \mu_i}{\partial x_j} + \frac{\partial \mu_j}{\partial x_i}\right) - \frac{2}{3}\rho k \delta_{ij} \tag{3}$$

In Eq. (3), μ_t presents the turbulent viscosity (kg.m^{-1}.s^{-1}) and k presents the turbulent kinetic energy (m^2.s^{-2}):

$$k = \frac{1}{2}\overline{u_i' u_j'} \tag{4}$$

The following format can be used to express the energy equation:

$$\underbrace{u_j \rho C_p \frac{\partial T}{\partial x_j}}_{A} = \underbrace{\frac{\partial}{\partial x_j}[\lambda \frac{\partial T}{\partial x_j}]}_{B} \tag{5}$$

$$u_j \frac{\partial T}{\partial x_j} = \frac{\partial}{\partial x_j}[a \frac{\partial T}{\partial x_j}] \tag{6}$$

where, A is the convective variation of the fluid's internal energy, B is the internal energy variation by conduction and $a = \lambda / \rho c_p$ is the fluid thermal diffusity (m^2.s^{-1}).

The turbulence viscosity for the $k - \varepsilon$ turbulence model is given by:

$$\mu_t = \rho C_\mu \frac{k^2}{\varepsilon} \tag{7}$$

where C_μ is a constant and ε is the dissipation rate.

The turbulence viscosity for the $k - \omega$ turbulence model is calculated by:

$$\mu_t = \rho \frac{k}{\omega} \tag{8}$$

where ω is turbulent frequency.

3.2. Solver settings

The CFD simulations were conducted using ANSYS Fluent 17.0. The simulations utilized the shear-stress transport (SST) $k - \omega$ model in conjunction with the 3D steady Reynolds-Averaged Navier-Stokes (RANS) equations. Pressure-velocity coupling was managed by the SIMPLE algorithm. Second-order discretization techniques were applied to both the convection and viscous parts of the governing equations. Pressure interpolation was carried out using pressure interpolation. Convergence criteria were met when the residuals for the continuity and momentum equations dropped below 10^{-5}. Similarly, convergence was considered sufficient when the residuals for the energy equation approached values less than 10^{-6}.

3.3. CFD modeling

The first opening of the cabin in question, intended for introducing external airflow into the cabin prototype, is situated at a height of $h_1 = 0.095$ m from the floor. Conversely, the second opening serves the purpose of expelling the internal airflow within the cabin prototype, is positioned at a height of $h_2 = 1.2$ m above the first opening. Figure 2 provides a visual representation of various cabin configurations, with 'r' representing the roof height and 'L' representing the room length. The specific parameter settings for CFD modeling are presented in Table 1.

3.4. Mesh selection

The initial step in validating the CFD simulations involves selecting an appropriate mesh. In this regard, the ANSYS meshing module was employed to create a non-uniform grid distribution, with hexahedral cells having a higher node density near the walls and openings. Additionally, a dimensionless wall distance (y+) of less than 5 was employed to facilitate the application of the SST $k - \omega$ turbulence model as shown in Fig. 3(a).
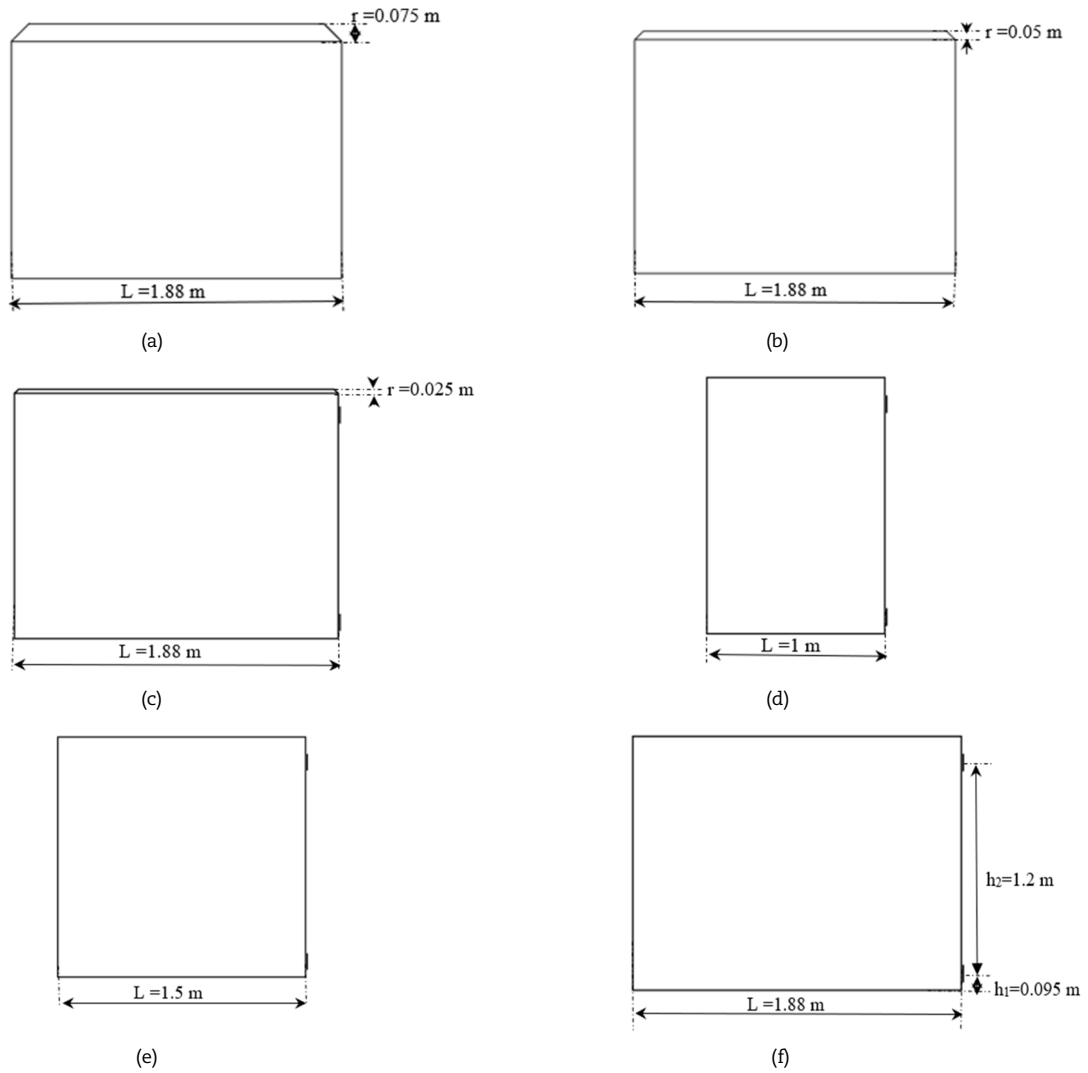
Fig. 2. The computational domain used for the various analyzed scenarios, (a) $r = 0.075$ m and $L = 1.88$ m, (b) $r = 0.05$ m and $L = 1.88$ m (c) $r = 0.025$ m and $L = 1.88$ m, (d) $r = 0$ m and $L = 1$ m, (e) $r = 0$ m and $L = 1.5$ m, (f) $r = 0$ m and $L = 1.88$ m.

This section of the study focuses on assessing the impact of mesh resolution. To achieve this, four distinct refined grids, characterized by node counts of 34058, 69685, 123006, and 186005 were considered to evaluate the sensitivity of the grid. Figure 3(b) provides an illustration of velocity values at a location characterized by x = 0.144 m, y = 0.5 m, and z = 0.095 m for the various mesh configurations. It is clear from these results that the velocity values exhibit variations among the different meshes. When compared with the experimental findings, it becomes apparent that the third and fourth meshes closely approximate the experimental results.

To evaluate the influence of node number on the accuracy of numerical results and determine the level of mesh refinement required to achieve the desired accuracy, we introduced the Grid Convergence Index (GCI%) for various cell counts in terms of velocity, as shown in Table 2.

The Grid Convergence Index (GCI) is a method used to estimate the numerical error in computational fluid dynamics (CFD) simulations due to spatial discretization, such as grid size. It is calculated using the following formula [21]:

$$GCI = \left(\frac{f_{ref} - f_{coarse}}{f_{coarse}}\right) \times GCI factor \times 100\% \tag{9}$$

where f_{ref}: the quantity of air velocity computed on the fine grid, f_{coarse}: the same quantity computed on the coarse grid, and GCI factor is given by GCI factor = $2p - 1$, where p is the order of accuracy of the numerical scheme.

Table 1. The parameter setting for CFD modelling.

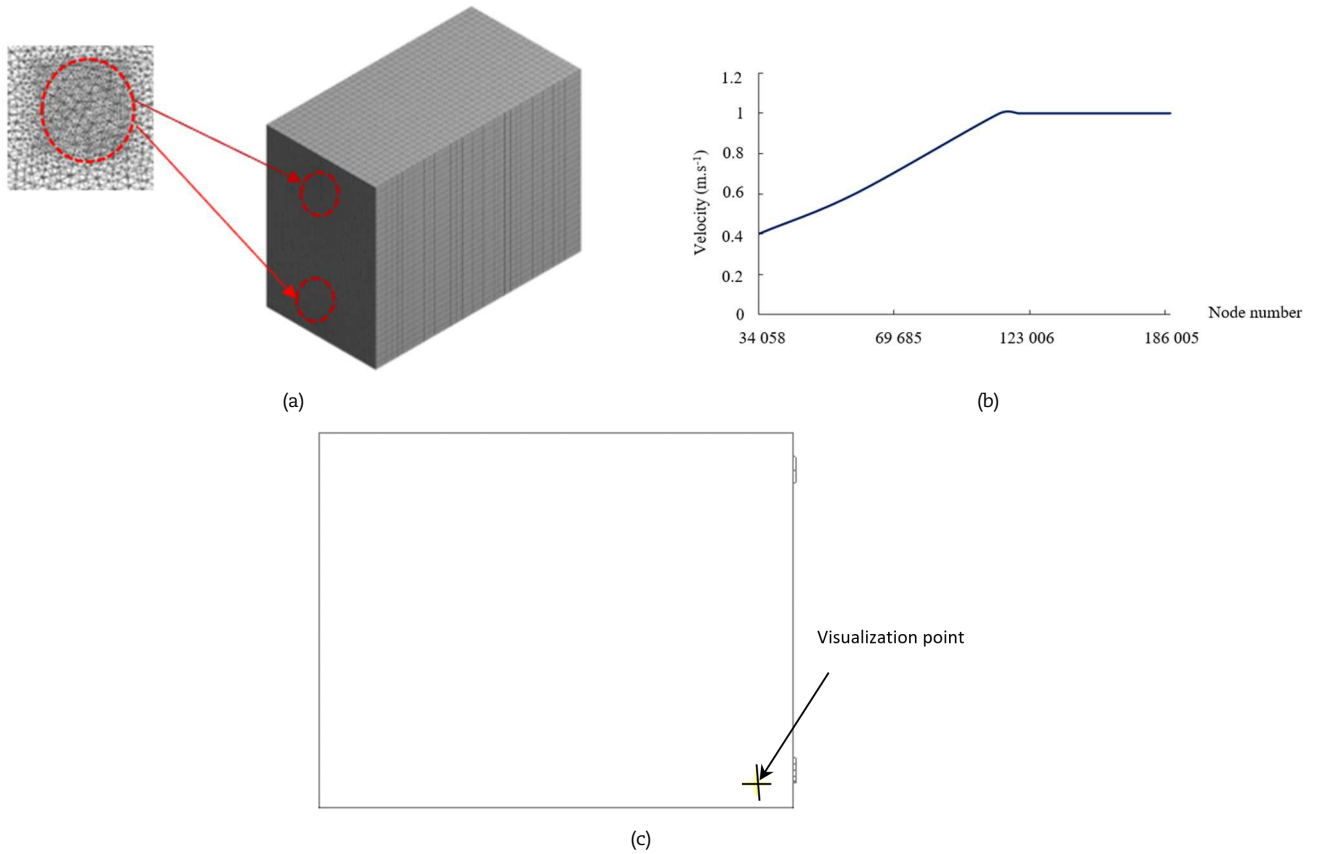|	Inlet velocity	Inlet temperature	Heat flux from walls	Cabin length (L)	Cabin roof height (r)
Case 1	$V = 1$ m.s^{-1}	$T = 301$ K	Adiabatic	$L = 1.88$ m	$r = 0.075$ m
Case 2	$V = 1$ m.s^{-1}	$T = 301$ K	Adiabatic	$L = 1.88$ m	$r = 0.05$ m
Case 3	$V = 1$ m.s^{-1}	$T = 301$ K	Adiabatic	$L = 1.88$ m	$r = 0.025$ m
Case 4	$V = 1$ m.s^{-1}	$T = 301$ K	Adiabatic	$L = 1$ m	$r = 0$ m
Case 5	$V = 1$ m.s^{-1}	$T = 301$ K	Adiabatic	$L = 1.5$ m	$r = 0$ m
Case 6	$V = 1$ m.s^{-1}	$T = 301$ K	Adiabatic	$L = 1.88$ m	$r = 0$ m

(a)

(b)

(c)

Fig. 3. Presentation of the mesh selection, (a) computational domain meshing, (b) velocity values at the location specified by x = 0.144 m, y = 0.5 m, and z = 0.095 m for various mesh configurations, (c) visualization of the point characterized by x = 0.144 m, y = 0.5 m, and z = 0.095 m.
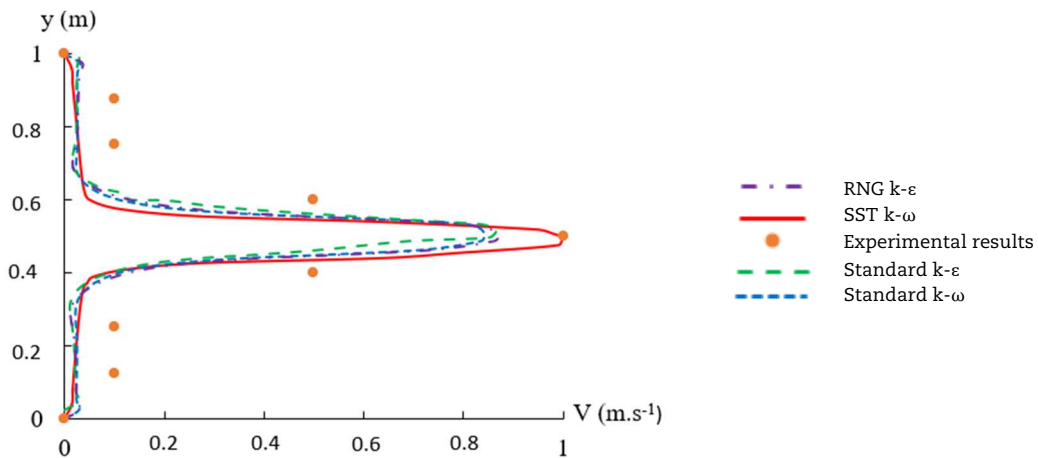

Fig. 4. Velocity profile along the direction characterized by x = 0.144 m and z = 0.095 m.

3.5. Turbulence model analysis

To determine the most suitable turbulence model, we compared four models: the standard $k-\omega$ model, the renormalization group $k-\varepsilon$ model (RNG $k-\varepsilon$), the shear-stress transport $k-\omega$ model (SST $k-\omega$), and the standard $k-\varepsilon$ model. Figure 4 illustrates the influence of the turbulence model on the velocity profile along the path defined by x = 0.144 m and z = 0.095 m. The results indicate that while the velocity profiles appear similar, the turbulence model significantly impacts the velocity values. Our findings show that the SST $k-\omega$ turbulence model provides the best agreement with our measurements, which were obtained using a prototype cabin, based on the numerical results.

Table 2. Meshing characteristics and dependency analysis.

Case	Node number	Cell number	Refinement factor (r)	GCI (%)
1	34058	31902	-	-
2	69685	65896	1.25	2.33
3	123006	117283	1.59	0.112
4	186005	174678	1.49	0.06

3.6. Comparison numerical and experimental findings

To substantiate the numerical results, a room with a length of L = 1.8 m and a roof height of r = 0 m was considered, and experimental data were collected using an anemometer of the Hot-wire type, as depicted in Fig. 1. Figure 4 illustrates a comparison of the numerical and experimental data for air velocity and air temperature along the direction specified by x = 0.144 m and z = 0.095 m. To assess the reliability of the experimental measurements, an uncertainty analysis was conducted using two metrics: the Mean Bias Error (MBE) [22] and the Coefficient of Variation of Root Mean Square Error (CVRMSE). Equation (10) is used to compute the MBE, in this equation, "d_i" stands for the point-to-point difference between the ith numerical result and the measured value, and "n" represents the total number of measurements.

The MBE values, defined in Eq. (10), were found to be approximately 0.057 for air velocity and 0.025 for air temperature, indicating good agreement between the experimental and numerical findings:

$$MBE = \frac{1}{n}\sum_{i=1}^{n}d_i \tag{10}$$

Additionally, in accordance with ASHRAE Guideline 14-2018, a CVRMSE below 25% is considered indicative of a satisfactory model fit with reliable predictive capabilities. The CVRMSE is computed using Eq. (11), where V_{exp_i} represents the experimental findings, V_{CFD_i} represents the numerical findings and N denotes the total number of data points.

The CVRMSE values were approximately 23% for air velocity and 16% for air temperature, further confirming the accuracy and reliability of the adapted numerical method:

$$CVRMSE = \frac{1}{V_{exp_i}}\sqrt{\frac{\sum_{i=1}^{N}\left(V_{CFD_i} - V_{exp_i}\right)^2}{N}} \tag{11}$$

Overall, these validation metrics demonstrate a high level of concordance between the experimental and numerical findings, reinforcing the accuracy of the numerical modeling approach.

4. Aerodynamic Properties of the Airflow

The present section delves into the analysis of airflow characteristics within the cabin across six distinct configurations, each defined by varying values of 'r' representing the roof height and 'L' signifying the length of the room. These analyses are conducted within the longitudinal plane characterized by y = 0.5 m. These different configurations offer insights into how changing the roof height and room length affects the airflow dynamics within the cabin.

4.1. Velocity fields

Figure 6 visually depicts the velocity fields for various room configurations. These visualizations reveal a consistent pattern across all considered configurations: The maximum flow velocity is attained at the inlet, where it is governed by a predefined velocity value of V = 1 m.s^{-1}, set as the inlet boundary condition. As the airflow progresses toward the opposite wall, a gradual deceleration is observed. In this region, the airflow bifurcates, resulting in the formation of a recirculation zone within the room. These findings underscore the significant impact of room configuration on the velocity fields. Specifically, it is evident that the maximum velocity value increases as the cabin length decreases and the roof height increases. For instance, V_{max} = 1.46 m.s^{-1} is observed for r = 0.075 m and L = 1.88 m, V_{max} = 1.44 m.s^{-1} for r = 0 m and L = 1.88 m, and V_{max} = 1.47 m.s^{-1} for r = 0 m and L = 1 m. In accordance with the numerical findings obtained from ANSYS Fluent 17.0, Eq. (12) represents the relationship between the maximum velocity value, room length (L), and roof height (r):

$$V_{max} = -0.032L + 0.1541\,r + 1.51 \tag{12}$$

This equation captures the evolution of the maximum velocity value as a function of these key room parameters, providing valuable insights into their interdependence.
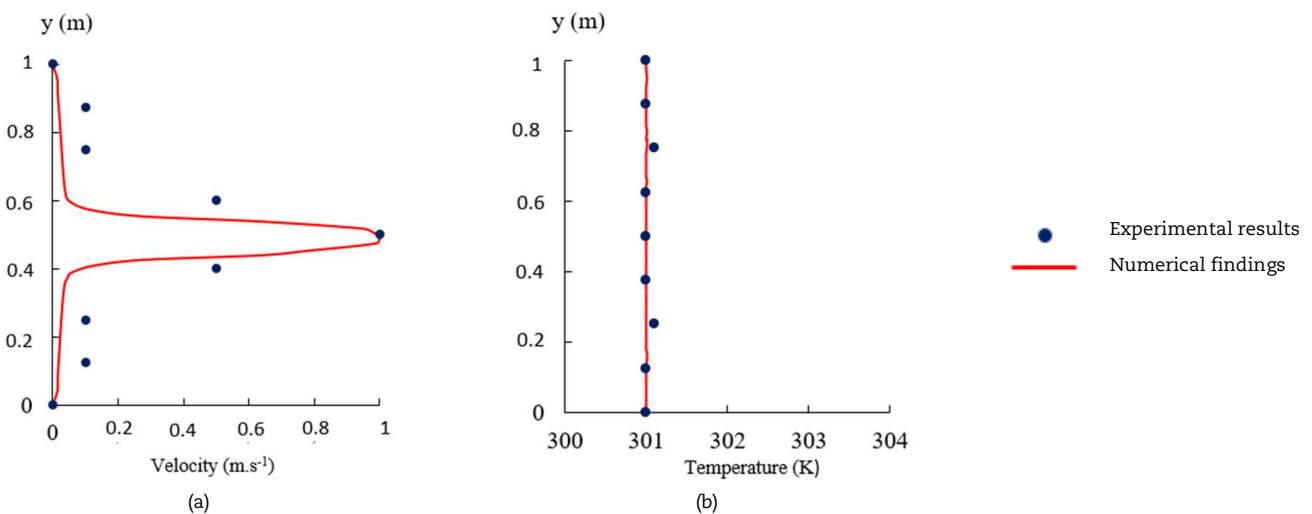

Fig. 5. Comparison the numerical and the experimental findings in the direction characterized by x = 0.144 m and z = 0.095 m, (a) air velocity profile, (b) air temperature profile
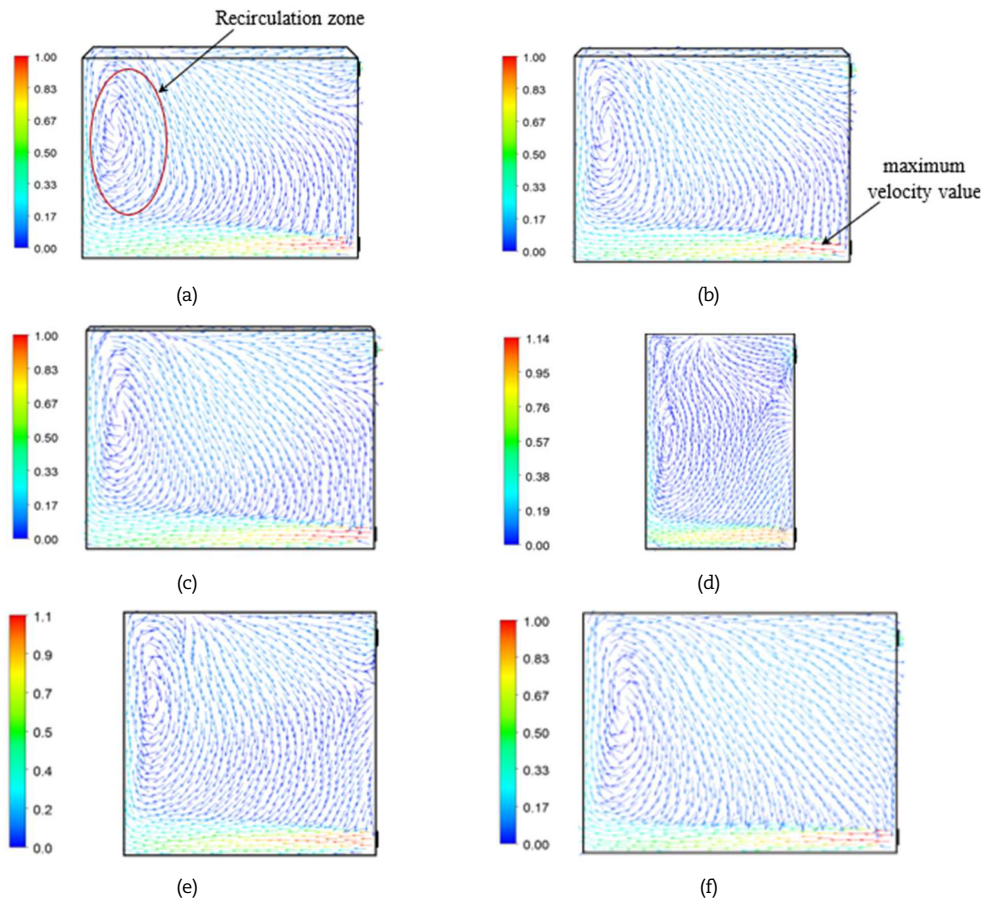
Fig. 6. Velocity field in the plane characterized by y = 0.5 m, (a) r = 0.075 m, L = 1.88 m, (b) r = 0.05 m, L = 1.88 m, (c) r = 0.025 m, L = 1.88 m, (d) r = 0 m, L = 1 m, (e) r = 0 m, L = 1.5 m, (f) r = 0 m, L = 1.88 m.

4.2. Static pressure

Figure 7 displays the static pressure contours for various room configurations, emphasizing the critical role of static pressure distribution in regulating indoor air quality, thermal comfort, and airflow resistance.

A notable observation across these configurations is the presence of a compression zone at the room's inlet. Subsequently, the static pressure remains relatively stable within the interior of the room, with higher static pressure values observed on the opposite side. Additionally, a depression zone is evident at the room's outlet. These results highlight the direct influence of room configuration on the static pressure contours. Specifically, it is evident that the maximum static pressure value increases as the cabin length increases, and the roof height rises. For example, P_{max} = 0.46 Pa is observed for r = 0.075 m and L = 1.88 m, P_{max} = 0.38 Pa for r = 0 m and L = 1.88 m, and P_{max} = 0.31 Pa for r = 0 m and L = 1 m.

In fact, analyzing the maximum static pressure allows researchers to identify areas of potential airflow stagnation or high airflow velocities. These factors are critical for designing efficient ventilation systems and ensuring indoor air quality. Static pressure measurements also help assess HVAC system performance and guide adjustments to optimize airflow distribution and comfort.

Hence, in accordance with the numerical findings obtained from ANSYS Fluent 17.0, Eq. (13) describes the connection between the maximum static pressure value, room length (L), and roof height (r):

$$P_{max} = 0.08L + 1.15r + 0.23 \tag{13}$$

This equation characterizes the evolution of the maximum static pressure value as a function of these key room parameters, providing valuable insights into their interplay.

4.3. Turbulent kinetic energy

A crucial factor in assessing indoor air quality and thermal comfort is the distribution of turbulent kinetic energy, which is shown in Fig. 8. Heat transmission, indoor pollutant dispersion, and air distribution patterns are all significantly influenced by turbulent kinetic energy. These visualizations reveal that k tends to have lower values throughout the entire room, with an increase in k values observed as one moves toward the outlet opening. Conversely, the highest k value is consistently found at the inlet opening. When focusing on the k value, it becomes evident that the configuration with r = 0 m and L = 1 m provides the highest turbulent kinetic energy. Specifically, the maximum value of turbulent kinetic energy increases as the cabin length decreases and the roof height increases. For instance, k_{max} = 0.115 $m^2.s^{-2}$ is observed for r = 0.075 m and L = 1.88 m, k_{max} = 0.082 $m^2.s^{-2}$ for r = 0 m and L = 1.88 m, and k_{max} = 0.118 $m^2.s^{-2}$ for r = 0 m and L = 1 m. In fact, by analyzing the maximum turbulent kinetic energy, researchers can identify regions within the room where turbulence is most intense. These areas often correspond to zones of high airflow velocity or areas of flow separation, which are important considerations for designing effective ventilation systems and assessing indoor air quality. In accordance with the numerical findings obtained from ANSYS Fluent 17.0, Eq. (14) characterizes the relationship between the maximum turbulent kinetic energy value, room length (L), and roof height (r):

$$k_{\max} = -0.04\,L + 0.43\,r + 0.158 \tag{14}$$

This equation provides valuable insights into how the maximum turbulent kinetic energy value evolves as a function of these key room parameters.
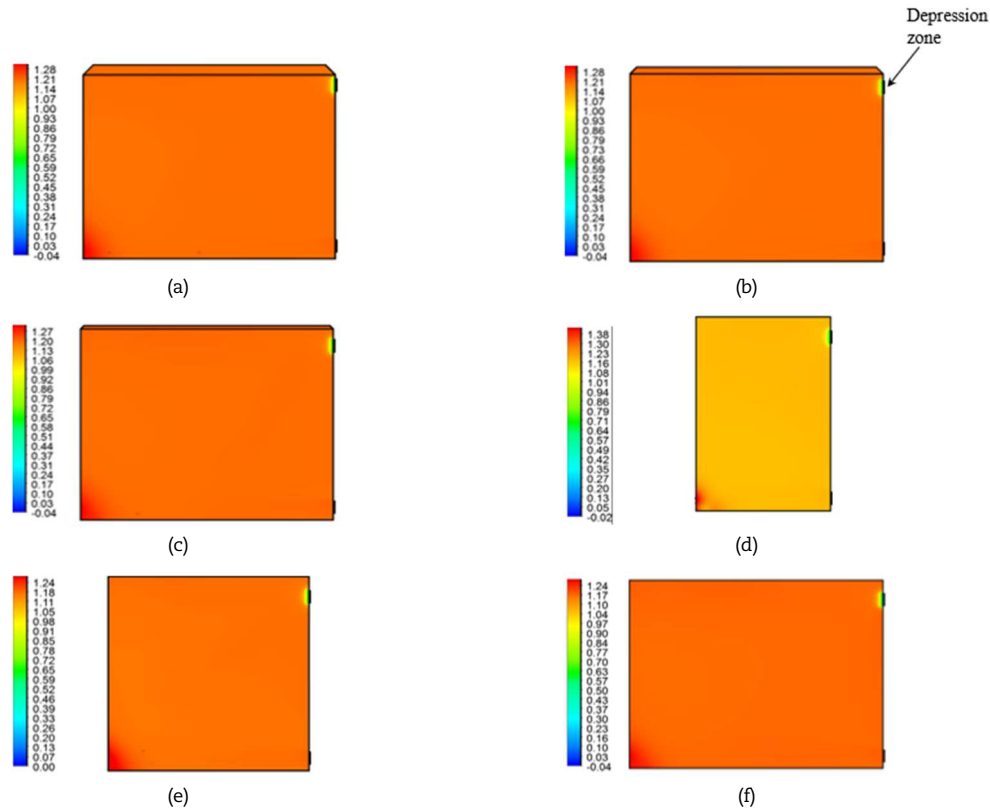

Fig. 7. Static pressure contour in the plane characterized by y = 0.5 m, (a) r = 0.075 m, L = 1.88 m, (b) r = 0.05 m, L = 1.88 m, (c) r = 0.025 m, L = 1.88 m, (d) r = 0 m, L = 1 m, (e) r = 0 m, L = 1.5 m, (f) r = 0 m, L = 1.88 m.
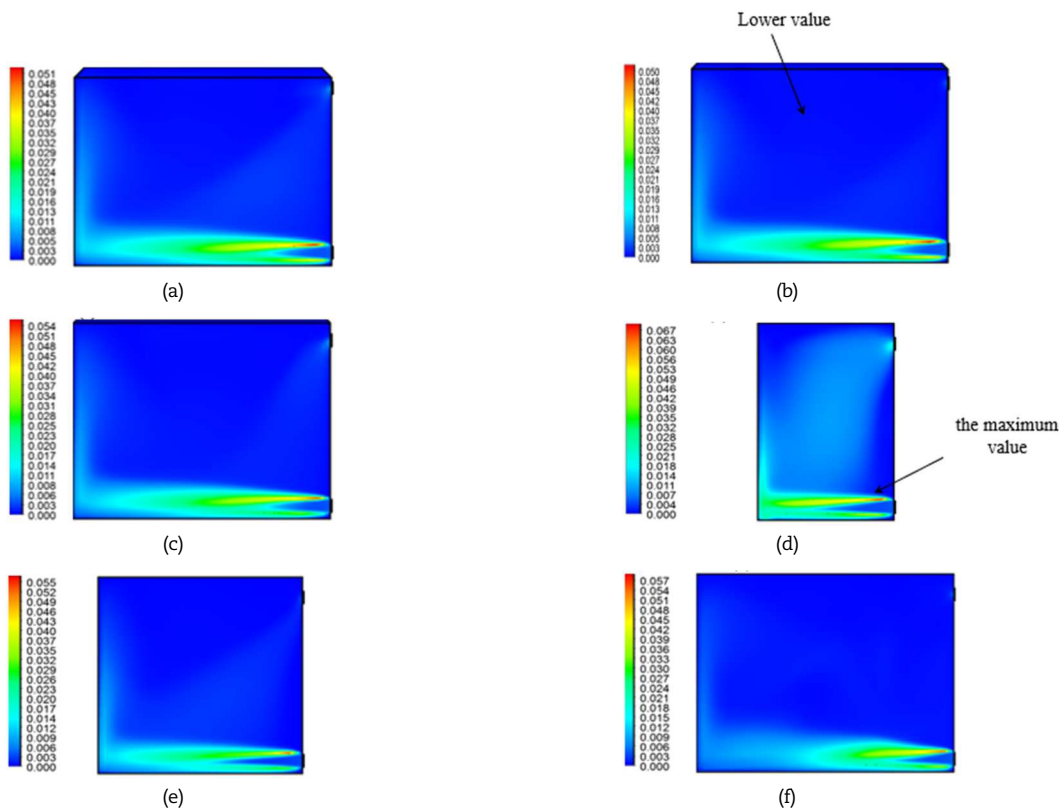

Fig. 8. Turbulent kinetic energy contour in the plane characterized by y = 0.5 m, (a) r = 0.075 m, L = 1.88 m, (b) r = 0.05 m, L = 1.88 m, (c) r = 0.025 m, L = 1.88 m, (d) r = 0 m, L = 1 m, (e) r = 0 m, L = 1.5 m, (f) r = 0 m, L = 1.88 m.

5. Heat Source Effect on Indoor Thermal Comfort

In this section, a thermal source was centrally positioned within the cabin under examination, as depicted in Fig. 9. Subsequently, four distinct numerical simulations were executed to investigate the impact of heat flux intensity on thermal comfort. The thermal source was subjected to various heat flux values, specifically $h = 150$ W.m^{-2}, $h = 300$ W.m^{-2}, $h = 500$ W.m^{-2} and $h = 800$ W.m^{-2}.

The Predicted Mean Vote (PMV) index serves as a pivotal metric for assessing thermal comfort [10], offering a numerical representation of the heat exchange between the human body and its surroundings. It spans a range from -3 to +3, indicating the spectrum from feeling cold to feeling hot. According to the ISO 7730 norm [23], indoor environments are classified as extremely comfortable when PMV values range between -0.5 and +0.5, and comfortable when they fall between -1 and +1. The PMV index is influenced by a multitude of factors, including metabolic rate, clothing insulation, air temperature, air velocity, and relative humidity:

$$PMV = (0.303 \times \exp(-0.036 \times M) + 0.028) \times (M - W) - 0.5 \times 10^{-3} \times (5733 - 6.99 \times M - Pa) - 0.42 \times (M - W - 58.15) \qquad (15)$$

where M is the metabolic rate of the person (expressed in watts per square meter), W is the external work being performed by the occupant (expressed in watts per square meter) and Pa is the partial pressure of water vapor in the air (expressed in kilopascals).
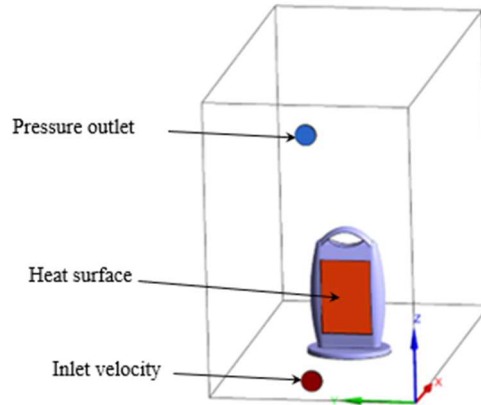

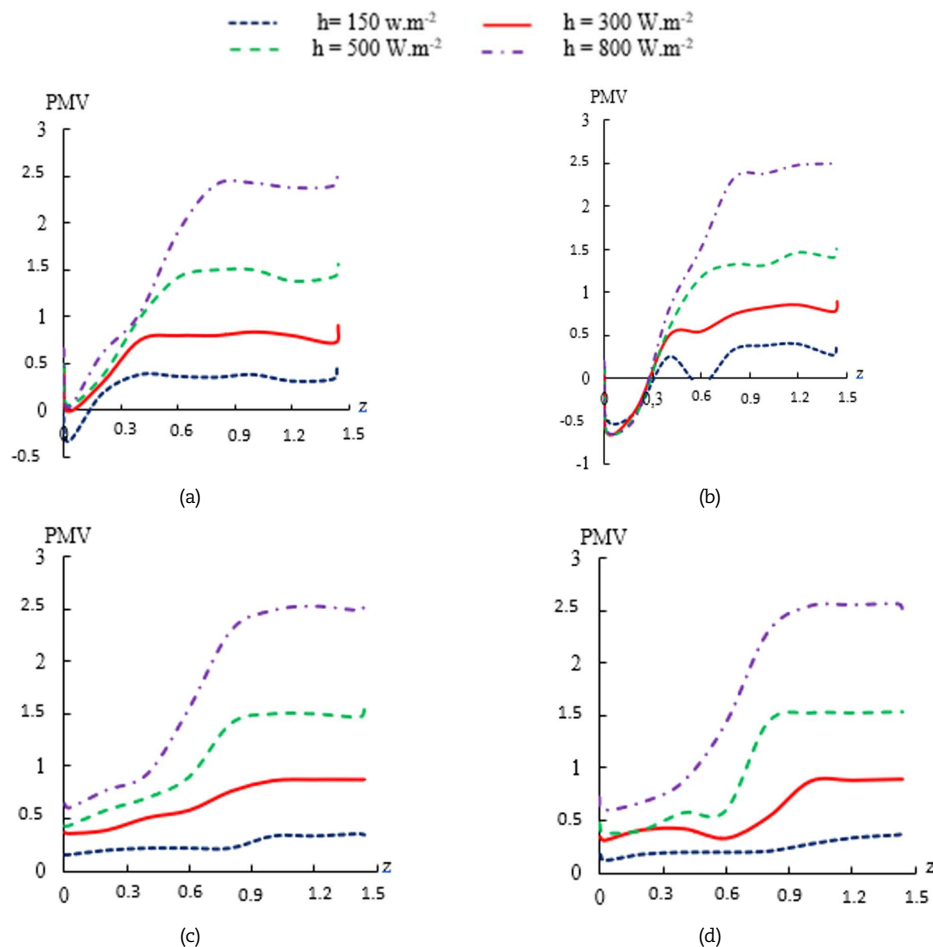**Fig. 9.** Geometrical arrangement.

Fig. 10. PMV profiles in the plane defined by y = 0.5 m, (a) x = 0.2 m, (b) x = 0.74 m, (c) x = 1.14 m, (d) x = 1.34 m.

In our study, we meticulously determined the air velocity and temperature for each scenario using Computational Fluid Dynamics (CFD) results, while maintaining a constant metabolic rate of 0.8 met, clothing insulation of 0.5 clo, and relative humidity of 50%. Figure 10 visually represents the PMV profiles for various heat flux intensities (h = 150 W.m^{-2}, h = 300 W.m^{-2}, h = 500 W.m^{-2}, and h = 800 W.m^{-2}) along the y = 0.5 m plane. These profiles vividly illustrate a direct correlation between heat flux intensity and PMV values, with higher intensities correlating to higher PMV values. For instance, the PMV remains below 0.45 for h = 150 W.m^{-2}, indicating a neutral thermal sensation. Conversely, it escalates to 2.55 for h = 800 W.m^{-2}, indicative of a warm thermal sensation.

6. Conclusion

This study investigated the impact of roof height and room length on indoor environments. The numerical results were validated using an experimental room prototype. A Grid Convergence Index (GCI%) analysis was conducted to determine the optimal mesh resolution, while a turbulence model selection study pointed to the SST $k-\omega$ model as the most suitable choice consistent with earlier research, thus affirming its applicability to the current study.

Based on the validated results, the following outcomes are drawn:

- Robust correlations are established to capture the variation of the aerodynamic parameters as function of cabin length and roof height. These correlations are in a good accordance with test data.
- The velocity fields distribution is influenced by geometrical parameters. As the cabin length diminishes (L = 1 m) and the roof height rises (r = 0.075 m), the maximum velocity experiences an increment.
- The static pressure distribution is influenced by geometrical parameters. The static pressure reached its maximum when the cabin length was 1.88 m and the roof height was 0.075 m.
- The study emphasizes the importance of considering the heat source on the indoor thermal comfort through numerical simulations conducted with different heat source.
- Along the plane characterized by y = 0.5 m and for different x-direction positions at x = 0.2 m, x = 0.74 m, x = 1.14 m, and x = 1.34 m, the PMV remains below 0.45 for h = 150 W.m^{-2}, indicating a neutral thermal sensation. Conversely, it rises to 2.55 for h = 800 W.m^{-2}, indicative of a warm thermal sensation.

Author Contributions

Hasna Abid: Conceptualization, Data curation, Formal analysis, Investigation, Methodology, Software, Validation, Visualization, Writing original draft; Ridha Djebali: Resources, Writing – review & editing; Hamza Faraji: Resources, Software, Writing, review & editing; Mariem Lajnef: Writing, review & editing; Zied Driss, Jamel Bessrour: Supervision, Writing, review & editing.

Conflict of Interest

The authors declared no potential conflicts of interest concerning the research, authorship, and publication of this article.

Data Availability Statements

All data generated or analyzed during this study are included in the published version.

References

[1] Zhang, S., Cheng, Y., Fang, Z., Huan, C., Lin, Z., Optimization of room air temperature in stratum-ventilated rooms for both thermal comfort and energy saving, *Applied Energy*, 204, 2017, 420–431.

[2] Akimoto, T., Tanabe, S., Yanai, T., Sasaki, M., Thermal comfort and productivity - Evaluation of workplace environment in a task conditioned office, *Building and Environment*, 45(1), 2010, 45–50.

[3] Shi, Z., Lu, Z., Chen, Q., Indoor airflow and contaminant transport in a room with coupled displacement ventilation and passive-chilled-beam systems, *Building and Environment*, 161, 2019, 106244.

[4] Li, X., Wang, X., Li, X., Li, Y., Investigation on the relationship between flow pattern and air age, *In: Sixth international IBPSA conference (Vol. II) IBPSA*, Kyoto, Japan, September 13–15, 1999.

[5] Shetabivash, H., Investigation of opening position and shape on the natural cross ventilation, *Energy and Buildings*, 93, 2015, 1-15,

[6] Farouk, M.I., Check the comfort of occupants in high rise building using CFD, *Ain Shams Engineering Journal*, 7(3), 2016, 953–958.

[7] Montazeri, H., Blocken, B., Derome, D., Carmeliet, J., Hensen, J.L.M., CFD analysis of forced convective heat transfer coefficients at windward building facades: Influence of building geometry, *Journal of Wind Engineering and Industrial Aerodynamics*, 146, 2015, 102–116.

[8] Driss, S., Driss, Z., Kammoun, I.K., Fluid Dynamic Investigation of the Height Effect of an Inclined Roof Obstacle, *International Journal of Fluid Mechanics & Thermal Sciences*, 1(1), 2015, 1-7.

[9] Peren, J.I., Van Hooff, T., Ramponi, R., Blocken, B., Leite, B.C.C., Impact of roof geometry of an isolated leeward sawtooth roof building on cross-ventilation: Straight, concave, hybrid or convex?, *Journal of Wind Engineering and Industrial Aerodynamics*, 145, 2015, 102–114.

[10] Fanger, P.O., Toftum, J., Extension of the PMV model to non-air-conditioned buildings in warm climates, *Energy and Buildings*, 34(6), 2002, 533-536.

[11] ISO 7730, Moderate Thermal Environments - Determination of the PMV and PPD Indices and Specifications of the Conditions for Thermal Comfort, 2nd Ed., International Standards Organisation, Geneva, Ref. No. ISO 7730:1994 (E), 1994.

[12] Ahmed, A.Q., Gao, S., Kareem, A.K., A numerical study on the effects of exhaust locations on energy consumption and thermal environment in an office room served by displacement ventilation, *Energy Conversion and Management*, 117, 2016, 74–85.

[13] Abid, H., Driss, Z., Bessrour, J., Study of the Aerodynamic Structure in an Indoor Environment Occupied by a Human Body, *International Journal of Mechanical and Mechatronics Engineering*, 19(3), 2019, 1-18.

[14] Chen, Z., Xin, J., Liu, P., Air quality and thermal comfort analysis of kitchen environment with CFD simulation and experimental calibration, *Building and Environment*, 172, 2020, 106691.

[15] Chaiyapinunt, S., Khamporn, N., Effect of solar radiation on human thermal comfort in a tropical climate, *Indoor and Built Environment*, 30, 2020, 391-410.

[16] Karava, P., Stathopoulos, T., Athienitis, A.K., Airflow assessment in cross-ventilated buildings with operable façade elements, *Building and Environment*, 46(1), 2011, 266-279,

[17] Zhong, H.Y., Yang, S., Jin, S., Qian, F.P., Zhao, F.Y., Kikumoto, H., Jimenez-Bescos, C., Liu, X., Single-sided natural ventilation in buildings: a critical literature review, *Building and Environment,* 212, 2022, 108797.

[18] Abid, H., Baklouti, I., Driss, Z., Bessrour, J., Experimental and numerical investigation of the Reynolds number effect on indoor airflow characteristics, *Advances in Building Energy Research*, 14(4), 2020, 424-449.

[19] Abid, H., Driss, Z., Computational study and experimental validation on the effect of inlet hole surface on airflow characteristics and thermal comfort in a box occupied by a thermal manikin, *International Journal of Ventilation*, 21(2), 2022, 140-156.

[20] Abid, H., Ketata, H., Lajnef, M., Chiboub, H., Driss, Z., Numerical investigation of greenhouse climate considering external environmental factors and crop position in Sfax central region of Tunisia, *Solar Energy,* 264, 2023, 112032.

[21] Baker, N., Kelly, G., O'Sullivan, P.D., A grid convergence index study of mesh style effect on the accuracy of the numerical results for an indoor airflow profile, *International Journal of Ventilation*, 19(4), 2020, 300-314.

[22] Abid, H., Zghal, O., Lajnef, M., Ketata, A., Zouari, S., Gugliuzza, G., Mejri, M., Arrabito, E., Driss, Z., Analysis of seasonal variations and their impact on the microclimate of soilless glass greenhouses: Numerical and experimental investigations, *Numerical Heat Transfer, Part A: Applications,* 2024, 1-25, DOI: 10.1080/10407782.2024.2320829.

[23] ASHRAE Guideline 14, ASHRAE Guideline 14-2014 for Measurement of Energy and Demand Savings, *American Society of Heating, Refrigeration and Air Conditioning Engineers*, Atlanta, GA, 2014.

ORCID iD

Hasna Abid https://orcid.org/0000-0003-2852-4853
Ridha Djebali https://orcid.org/0000-0002-1017-3410
Hamza Faraji https://orcid.org/0000-0003-2792-4986
Mariem Lajnef https://orcid.org/0000-0003-1577-9523
Zied Driss https://orcid.org/0000-0003-0397-1868
Jamel Bessrour https://orcid.org/0000-0002-0337-8215

Publisher's Note Shahid Chamran University of Ahvaz remains neutral with regard to jurisdictional claims in published maps and institutional affiliations.